ARTICLE

Check for updates

Massive earthquake swarm driven by magmatic intrusion at the Bransfield Strait, Antarctica

Simone Cesca [1✉], Monica Sugan [2], Łukasz Rudzinski[3], Sanaz Vajedian[4], Peter Niemz[1,5], Simon Plank[6], Gesa Petersen [1,5], Zhiguo Deng[1], Eleonora Rivalta[1,7], Alessandro Vuan [2], Milton Percy Plasencia Linares [2], Sebastian Heimann[5] & Torsten Dahm[1,5]

An earthquake swarm affected the Bransfield Strait, Antarctica, a unique rift basin in transition from intra-arc rifting to ocean spreading. The swarm, counting ~85,000 volcano-tectonic earthquakes since August 2020, is located close to the Orca submarine volcano, previously considered inactive. Simultaneously, geodetic data reported up to ~11 cm north-westward displacement over King George Island. We use a broad variety of geophysical data and methods to reveal the complex migration of seismicity, accompanying the intrusion of 0.26–0.56 km^3 of magma. Strike-slip earthquakes mark the intrusion at depth, while shallower normal faulting the ~20 km long lateral growth of a dike. Seismicity abruptly decreased after a Mw 6.0 earthquake, suggesting the magmatic dike lost pressure with the slipping of a large fault. A seafloor eruption is likely, but not confirmed by sea surface temperature anomalies. The unrest documents episodic magmatic intrusion in the Bransfield Strait, providing unique insights into active continental rifting.

[1] GFZ German Research Centre for Geosciences Potsdam, Potsdam, Germany. [2] National Institute of Oceanography and Applied Geophysics – OGS, Trieste, Italy. [3] Institute of Geophysics, Polish Academy of Sciences, Warszawa, Poland. [4] Missouri University of Science and Technology, Department of Geosciences and Geological and Petroleum Engineering, Rolla, MO, USA. [5] Institute of Geosciences, University of Potsdam, Potsdam-Golm, Germany. [6] German Aerospace Center (DLR), Oberpfaffenhofen, Weßling, Germany. [7] University of Bologna, Bologna, Italy. ✉email: simone.cesca@gfz-potsdam.de

In August 2020 an intense seismic swarm started at the Bransfield Strait, Antarctica[1], with 128 events exceeding Mw 4.0[2,3]. During its early phase 3,186 earthquakes were reported, based on the analysis of seismic data at a local station[1]. The swarm peaked with two large earthquakes on 2 October (Mw 5.9) and 6 November (Mw 6.0) 2020, before tapering off. By February 2021 the seismic activity was substantially reduced. The estimated seismic moment released from August 2020 to February 2021 was ~3.88 × 10^18 Nm (equivalent to Mw 6.4). The seismicity is localized close to the Orca seamount, a seafloor caldera shield volcano of 900 m bathymetric height offshore the coast of King George Island, where earthquakes were felt at Antarctic bases. While the nearby plate boundaries and rift are seismically active[4,5] and hosted swarm episodes of presumed magmatic origin[4,6,7], earthquakes are typically moderate[2,3]. Due to region remoteness, seismic instrumentation scarcely covers the Bransfield Basin. Temporary experiments, including ocean-bottom sensors, were carried out on recovering seismicity features[7]. There was no evidence of similar volcanic swarms in the past experiments: even if the off-shore volcanism and extensional tectonics could sometimes increase the seismic rate in the back-arc basin, a comparably energetic swarm has never been recorded in the region (Fig. 1).

The South Shetland Islands––Antarctic Peninsula region hosts the remnant segment of a formerly larger subduction zone, which is today limited to the Phoenix block segment. The Bransfield Basin, which separates the South Shetland Islands and the Antarctic Peninsula, is not a "normal" back-arc basin[8]. It lies in a unique tectonic environment. Although active subduction occurred during most of the past 200 m.y., it slowed dramatically at about 4 Ma when the Phoenix-Antarctic spreading center was abandoned offshore, leaving a small remnant of the former Phoenix plate incorporated in the Antarctic plate. Even though geochemical data indicate that unaltered basalt dredged from the Bransfield basin is like midocean ridge basalt, there is no clear evidence for normal seafloor spreading. Continental crust is thinning to develop oceanic crust[9,10]. The current extension in the NE trending Bransfield Strait back-arc basin at the rifting-spreading transition[11,12] is either attributed to the Phoenix Block subduction and rollback or to shear between the Scotia and Antarctic plates[4]. This is supported by transtensional focal mechanisms[7,13,14], a neovolcanic zone with major volcanic centers[4,9,15,16] and heat flow anomalies[11,16,17]. The spreading rate has been quantified as 1.0 cm/yr[18] and 0.9–2.4 cm/yr[4] based on GNSS and magnetic anomaly data, respectively. The extension focuses on the NW side of the basin, close to the South Shetland Islands shoreline[19]. The crust is 9-10 km thick in the central basin, increasing to 14–16 km towards SW[7,10,12,19–21]. The development of the Bransfield Strait basin underwent different phases: an increase of tensional stresses and local crust splits, the formation of graben-like structures, intensive explosive activity at the growing volcanic edifices, and localized volcanic activity along an elongated, narrow band of neovolcanic features[22]. The seafloor morphology comprises different basins[22]. The Central basin, extending ~250 km between Deception and Bridgeman Islands. It hosts a number of volcanic features and seamounts, either presenting isometric structures with elongated ridge-parallel features, at one (Orca seamount) or both (Ex seamount) sides, or complex ridge-parallel structures (Three Sisters seamount)[9,15,22]. The Orca seamount has a nearly circular cone, with a basal diameter of 11 km, a height of ~900 m and a 3 km wide caldera of 350 m depth, with pronounced spurs off the main building extending SW[23].

Seismic swarms at volcanic centers or fissure-like ridges[1], hydrothermal activity[12,17,24,25], and basalt younger than 0.1 Ma[26] show that the Bransfield Strait is volcanologically active. Orca volcano samples revealed subalkaline basalts and basaltic

andesites, with different proportion of young glass[11]. While the Orca seamount is considered to be inactive[23], biological samples[17] provide evidence for past magmatic activity and a shallow hydrothermal system. Low velocity zones in the mantle wedge suggest widespread partial melting[10,21]. Temporal amphibious deployments provided additional information in the region of the Orca seamount. Seismicity analysis revealed swarm episodes with suggested magmatic origin at the seamount and its NE flank[4–7]. Preliminary results of tomography and refraction studies suggested magma accumulation at shallow depth beneath the Orca seamount[27].

Regional seismicity is mostly shallow; sporadic deeper earthquakes (down to 65 km depth) mark the remnant subduction[7]. Thrust events are located in the forearc, while strike-slip and normal faulting events are common in the back-arc, confirming the local transtensional tectonics. The Bransfield basin seismicity has been moderate (Fig. 1).

Here we analyse regional seismological data, ground displacement from InSAR and two local GNSS stations (Supplementary Notes 1, 2, 3, Supplementary Fig. 1), and sea surface temperature and roughness data. We model the seismo-geodetic data to reconstruct the spatiotemporal evolution of seismo-volcanic processes, which are attributed to a magma intrusion through the crust.

Results

Analysis and modeling of seismogeodetic data. In Antarctica, global seismic catalogs can be considered complete only for events stronger than $M = 4.0$, due to the sparse regional seismic stations coverage. We applied a range of modern, waveform-based seismological techniques[28–32] to augment the number of detected earthquakes and track and characterize the seismological sequence. We detect ~85,000 earthquakes over 6 months and locate ~6,000 (Figs. 2, 3, Supplementary Note 4, Supplementary Fig. 4, Supplementary Dataset 1) by processing continuous recordings of local stations (Supplementary Fig. 1) using single station techniques. Our results antedate the unrest to August 10, 2020 (time t_1, Fig. 3). The seismicity rate is initially low, but increases substantially in rate and magnitude at the end of August. We depict a complex migration pattern (Fig. 3), which we analyse in detail below.

We model regional waveform data to perform earthquake source inversions[29], resolving moment tensor, rupture type, centroid location, depth and moment magnitude for 84 earthquakes (Supplementary Note 5, Supplementary Figs. 5, 6, Supplementary Dataset 2) as well as their uncertainties (Supplementary Fig. 7). Two families of moment tensors are identified[31] (Supplementary Note 6): predominant strike-slip mechanism and normal faulting (Supplementary Fig. 8). The tension axes of both earthquake types are oriented NW-SE (Fig. 2), consistent with the regional tectonics and the opening of the Bransfield Strait. The average centroid location is in agreement with global solutions[2,3] and locate the focal region between the Orca volcano and King George Island. We resolve further details of the seismicity distribution: strike-slip events are spatially clustered NE of the Orca volcano, while normal faulting events further extend along a narrow band oriented NE-SW. Centroid depths, which are resolved with an average uncertainty of 2–3 km, indicate that the seismicity is shallow, rarely exceeding 15 km. Strike-slip earthquakes are slightly deeper and stronger (average depth 9 ± 2 km, magnitudes up to Mw 6.0), compared to normal faulting (average depth 7 ± 2 km, magnitudes up to Mw 5.1). Robust non double couple components (Supplementary Figs. 5, 7) consistently show a positive compensated linear vector dipole (CLVD) and, in the case of normal faulting earthquakes, a
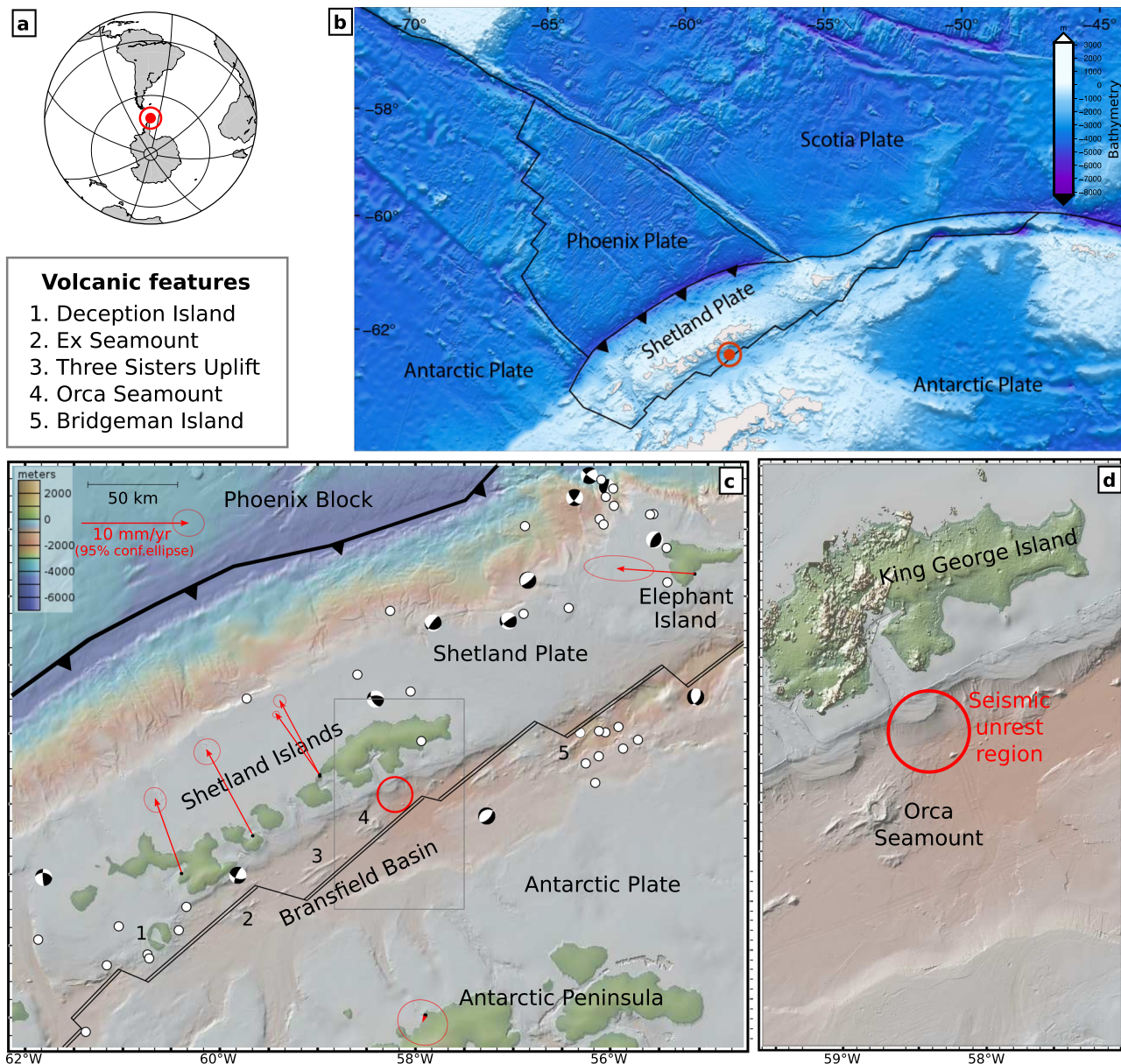
Fig. 1 South Shetland Island map. a Globe showing the location of the study region (red circle). **b** Regional map showing the tectonic setting (red circle denotes the location of the swarm). **c** Map of the Brainsfield Basin, between Shetland Islands and Antarctic Peninsula. The regional seismicity was moderate prior to the unrest (white circles are earthquakes with magnitudes M5+ from the USGS catalog in the period 1971–2020, focal mechanisms are centroid moment tensor solution from the Global CMT catalog in the period 1976–2020). Red arrows indicate the background horizontal ground velocity relative to Antarctica at GNSS sites[35] showing NW-SE extension in the Bransfield Strait (ellipses show 95% confidence regions[35]). A rectangle denotes the extent of the local map (panel **c**) and a red circle the average location of the unrest seismicity (based on the USGS seismic catalog). Major regional tectonic features are the subduction of the Phoenix Block (the thick solid line marks the Phoenix-Shetland plate boundary[79]) and the active rift along the Bransfield Basin (thin double black line and single line mark active ridge and transform fault segments, respectively, after the University of Texas Institute for Geophysics, UTIG, database). **d** Local map showing the bathymetric details and the Orca seamount building next to the region of the unrest (red circle). Panels c and d have been plotted with GeoMapApp (www.geomapapp.org)[80], using the Global Multi-Resolution Topography (GMRT).

positive isotropic component (Supplementary Figs. 7, 8), implying a combination of shear and opening tensile failures[33].

The application of template matching techniques bridges the regional and local analyses (Supplementary Note 7, Supplementary Fig. 9, Supplementary Dataset 3): given their waveform similarity we attribute the focal mechanism and location of the respective templates to the newly detected events[34] (Supplementary Note 8, Supplementary Figs. 10, 11). The overall temporal evolution depicts an alternation of strike-slip and normal faulting earthquakes and helps to track the migration of seismicity (Fig. 3, Supplementary Figs. 11, 12).

GNSS (stations DAL5, UYBA) and InSAR data along King George Island coastline show a transient surface deformation from August 2020 and persisting over months superposed to the background spreading rate, which we estimate as 2.1 cm/yr at UYBA. Ice cover prevents the InSAR analysis within the island. The transient, quantified after accounting for the slow spreading of the Bransfield rift at GNSS stations[35], indicates continuous ~N62.9°W horizontal motion, away from the seismogenic region (Fig. 3, Supplementary Fig. 13, Supplementary Note 9), reaching 10.7 ± 1.0 cm and 6.4 ± 1.3 cm over 6 months at DAL5 and UYBA, respectively. A minor uplift of 1.3 ± 0.2 cm is resolved at DAL5.
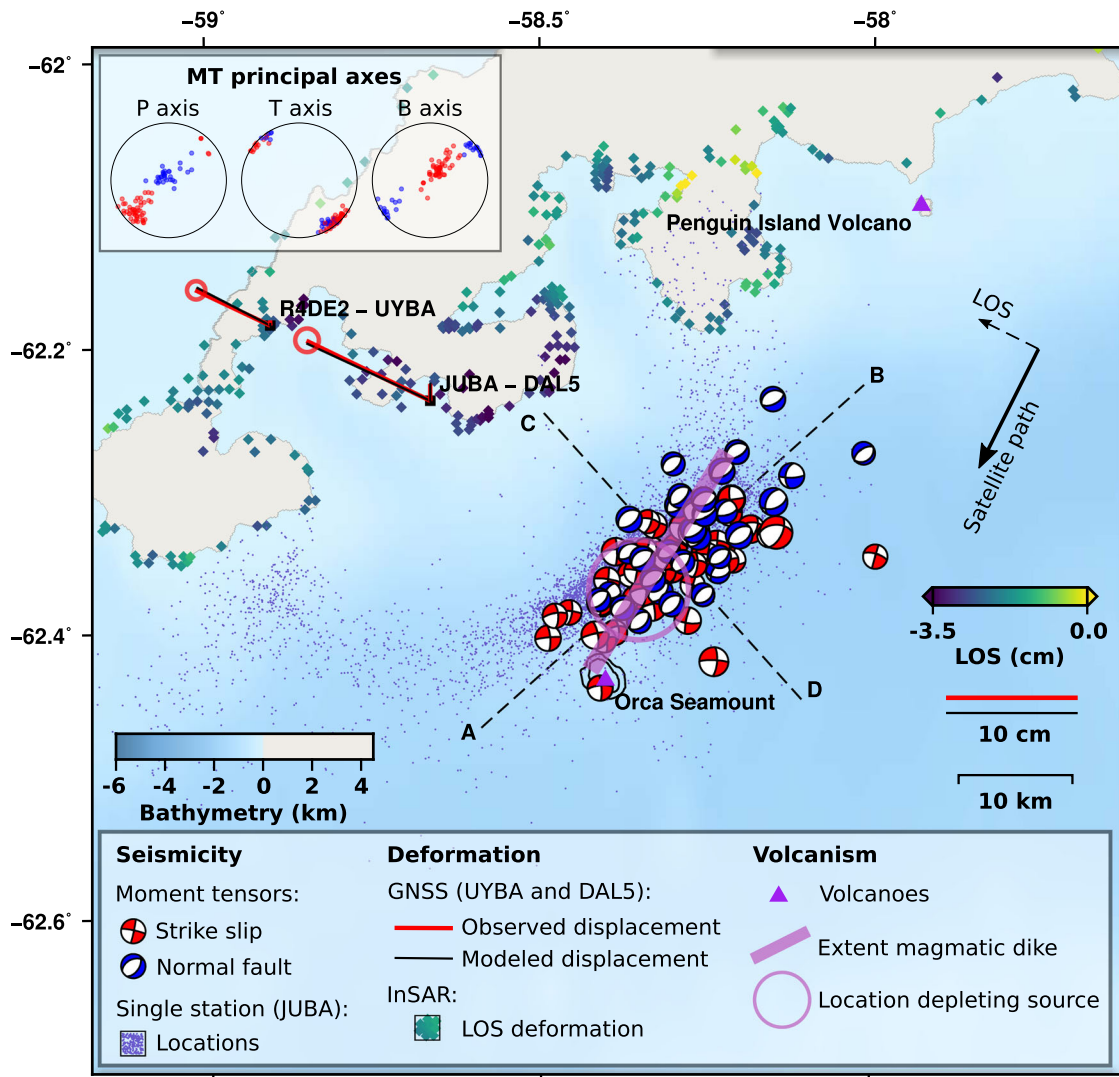
Fig. 2 Overview of seismological and geodetic observations and results. Seismological results include centroids, double couple components of moment tensors, and distribution of principal axes, based on regional data, and locations from the single-station approach. Geodetic modeling results include the locations of the depleting source and sub-vertical dike and the corresponding fit of GNSS cumulative displacement from 1 August 2020 to 1 February 2021 (horizontal uncertainty ellipses are plotted for 1 standard deviation, while the corresponding vertical uncertainties are 0.2 and 0.3 cm at DAL5 and UYBA, respectively), together with the downsampled spatial distribution of displacements along the line of sight (LOS) from InSAR processing (for the time period of 17 July 2020 to 6 February 2021); due to the different orientation of satellite trajectory and displacement vectors, LOS displacement projections are smaller than absolute displacements recorded by GNSS data. Local stations JUBA (seismic) and DAL5 (GNSS) are located at the Carlini Antarctic base (Argentina) and R4DE2 (seismic) and UYBA (GNSS) at the Artigas Antarctic base (Uruguay).

The modeled displacements due to the cumulative effect of the largest earthquakes reproduce the observed orientations, but only accounts for ~1–4% (1–3 mm) of observed amplitudes (Supplementary Fig. 14). Given the history of the volcanic activity in the area, we propose that a magma intrusion is mainly responsible for the observed surface displacements. The high correlation among the deformation time series and the cumulative number of normal faulting events (Fig. 3) suggests that both seismicity and deformation are controlled by the same process, which we hypothesize to be a sub-vertical dike intrusion. The observed deformation is well explained by the opening of a sub-vertical magmatic dike. This can be modeled by means of a tensile dislocation source[36] (Supplementary Note 10, Suppl. Tabs. 2, 3), whose location and orientation was constrained by the normal faulting activity above it (Fig. 2, Supplementary Fig. 7). The tensile source resolved by geodetic data, the presence on positive non-DC terms in focal mechanisms, and the alignment and

extent of normal faulting all consistently give evidence for a sub-vertical dike beneath these events: earthquakes with normal faulting mechanisms are triggered above a vertical dike while their spatial distribution provides an indirect evidence for the dike lateral growth[37,38]. Deeper strike-slip events are likely the response to magma intrusion deeper in the crust during the initial opening of the feeder dike and later magma inflow. Since the magmatic intrusion must be fed at larger depth, beneath strike-slip seismicity, we additionally model a depleting magma chamber feeding the dike. To this purpose we assume a volumetric source at a depth of 20 km and at the average location of early strike-slip templates. GNSS data are best modeled for a sub-vertical dike with a centroid at −62.35°N, −58.32°E, at 13 ± 1 km depth. The lateral NE-SW elongation of the dike is independently supported by the spatial distribution of normal faulting epicenters (oriented ~N48°E) and their median strike angle (~N52°E). These values are coherent with the NW-SE
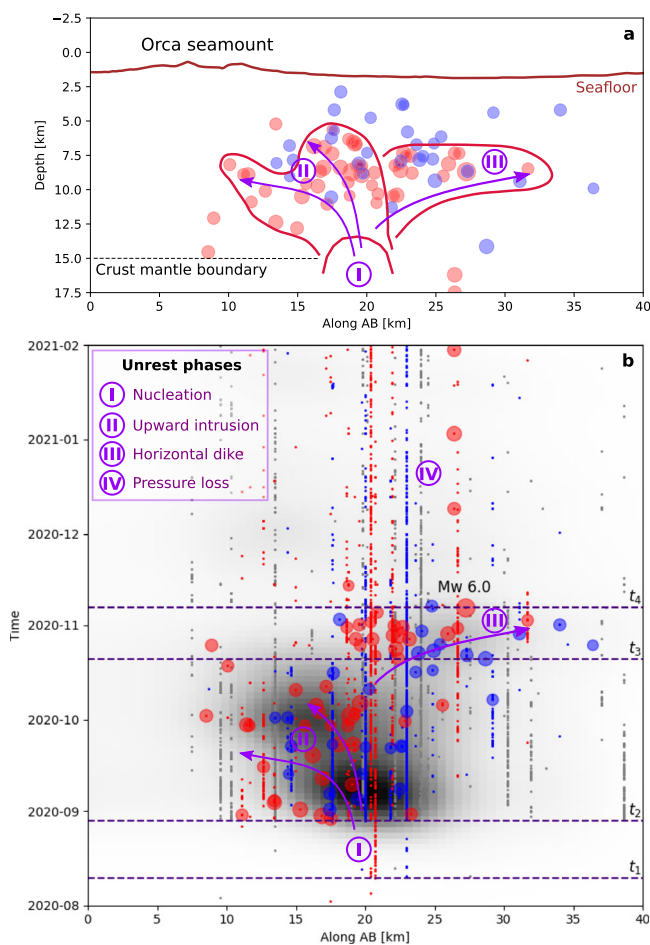
Fig. 3 Summary cartoon of the volcano-tectonic unrest. a Vertical cross-section along profile AB (Fig. 2), with strike-slip events (red) marking the magma path (arrows) in different phases (numbers), and normal faulting events (blue) being triggered above the lateral dike intrusions. **b** Temporal evolution of seismicity along profile AB, based on moment tensor solutions (circles), template matching (only events with threshold at 12 times the MAD and cross correlation values above 0.55 are shown) and single station analysis (grayscale kernel density plot). Horizontal indigo dashed lines mark the starting time of four phases of the unrest that are recognized: weak seismicity unrest marking the location of the depleting reservoir off the Orca seamount, below 15 km depth (phase I), upward and SW migration (phase II), further magma flux and formation of a horizontal dike towards NE (phase III) and seismicity drop, following the largest Mw 6.0 earthquake and dike pressure drop (phase IV).

horizontal direction of the tension axes of moment tensor solutions, implying a tensile opening component roughly perpendicular to the strike. The dike volumetric change corresponds to an intrusion of up to $0.56 \pm 0.04 \times 10^6\,\text{km}^3$ of magma, while the same volume is depleted at depth. The lower extent of the dike is hardly constrained by the seismic activity, but its top should be at ~5-10 km depth, confined below the normal faulting earthquakes (Fig. 4), which have an average depth of 7 ± 2 km. Consistently, the dike geometry constrained by the geodetic modeling, with a slightly deeper average depth (13 km) and a width of 12 ± 3 km (Supplementary Tab. 2), suggests the dike top at depth of 7 ± 3 km. InSAR data provides coherent LOS displacement timelines as GNSS at station locations (Supplementary Fig. 15). The ice/snow coverage limits the robust analysis of InSAR to 326 data points, downsampled from 6,754 pixels, mostly located along King George Island's coastline (Fig. 2). This

is sufficient to constrain the dike extent to ~20 km (Supplementary Fig. 16), which cannot be resolved using the two GNSS stations alone.

Chronology of the seismo-volcanic unrest. In the 6-months time period from 1 August 2020 to 1 February 2021, when the seismicity and deformation rates were highest, we identify 4 phases of the sequence (Figs. 3, 4). Phase 1 (10–29 August 2020) is characterized by a low seismicity rate and weak earthquakes (M < 3). Single station (Fig. 3c, d) and template matching (Fig. 3e) analyses suggest that this early seismicity is located at 10–15 km depth, in the region where strike-slip earthquakes will later cluster. This appears as the first sign of unrest, possibly in response to deep magma migration at the crust-mantle boundary from a deeper reservoir. Seismicity occurs within a compact seismogenic volume in Phase 1, with little or no lateral migration. No clear deformation signal is found at this time (Fig. 3G), implying a magmatic intrusion is not yet formed, or too deep and/or weak to be detected. Phase 2 starts on 29 August 2020, with the first large earthquakes (M 4.5+) reported by international agencies[2,3]. Seismicity increases in rate and magnitude (Fig. 3a, f), while the deformation transient becomes visible at both GNSS stations (Fig. 3g, Supplementary Fig. 13). Deeper strike-slip events are soon accompanied by shallower normal faulting, the first large one occurring ~3 days after the onset of phase 2 (Fig. 3a). This observation suggests a fast (~3–4 km/day) upward migration of the magma dike. A lateral migration is also depicted at this time, both revealed by the backazimuths estimated from the single station analysis (Fig. 3c) and by centroid locations of large earthquakes (Figs. 2, 3b). This implies that the intrusion first migrates SW towards the Orca seamount, where it eventually stops. Such path geometry, first propagating sub-vertically upward and then bending laterally towards the Orca seamount, can be qualitatively explained in the light of shallow local stresses due to the seamount load[39–41]. In the last part of phase 2, the seismicity slowly decreases (Supplementary Fig. 9b), as the intrusion stops while approaching the volcanic edifice, possibly inhibited by different host rock density[42] or by the load of the volcanic edifice[43]. We identify the beginning of phase 3 by 21 October 2021, when a new burst of strike-slip earthquakes occurs. Such increase in seismicity may be either attributed to additional magma inflow from depth or to the dike propagation within a more cold and brittle region, followed by normal faulting events migrating towards NE, i.e. away from Orca seamount. The NE-SW band of normal faulting with a similar strike direction, further extending towards NE, is a typical sign for a sub-vertical magmatic dike. The dike would lay beneath these earthquakes, thus propagating over a total length of ~20 km. Increased magma inflow in phase 3 may have been favored by unloading[44] after ice melting at King George Island accompanying the seasonal temperature increase, which is testified by sea temperature increases and sea ice coverage decrease in this phase (Supplementary Fig. 17). Unloading effects may also have affected deformation data. Phase 3 terminates with the largest event of the sequence on 6 November 2020 (Mw 6.0). After this date (Phase 4), the seismicity and the deformation signal drop rapidly (Fig. 3f, g). Our interpretation is that, following the failure of a large, shallow fault, the dike looses pressure and is inhibited to further propagate. Indeed, it has been long recognized from field observations and numerical models[45–49] that dikes tend to slow down or even get arrested when they induce large earthquakes. This is because the earthquakes represent sinks of inelastic energy[46] and increase the fracture energy necessary for further propagation; this in turn decreases the elastic energy available for propagation, and thus also the dike's
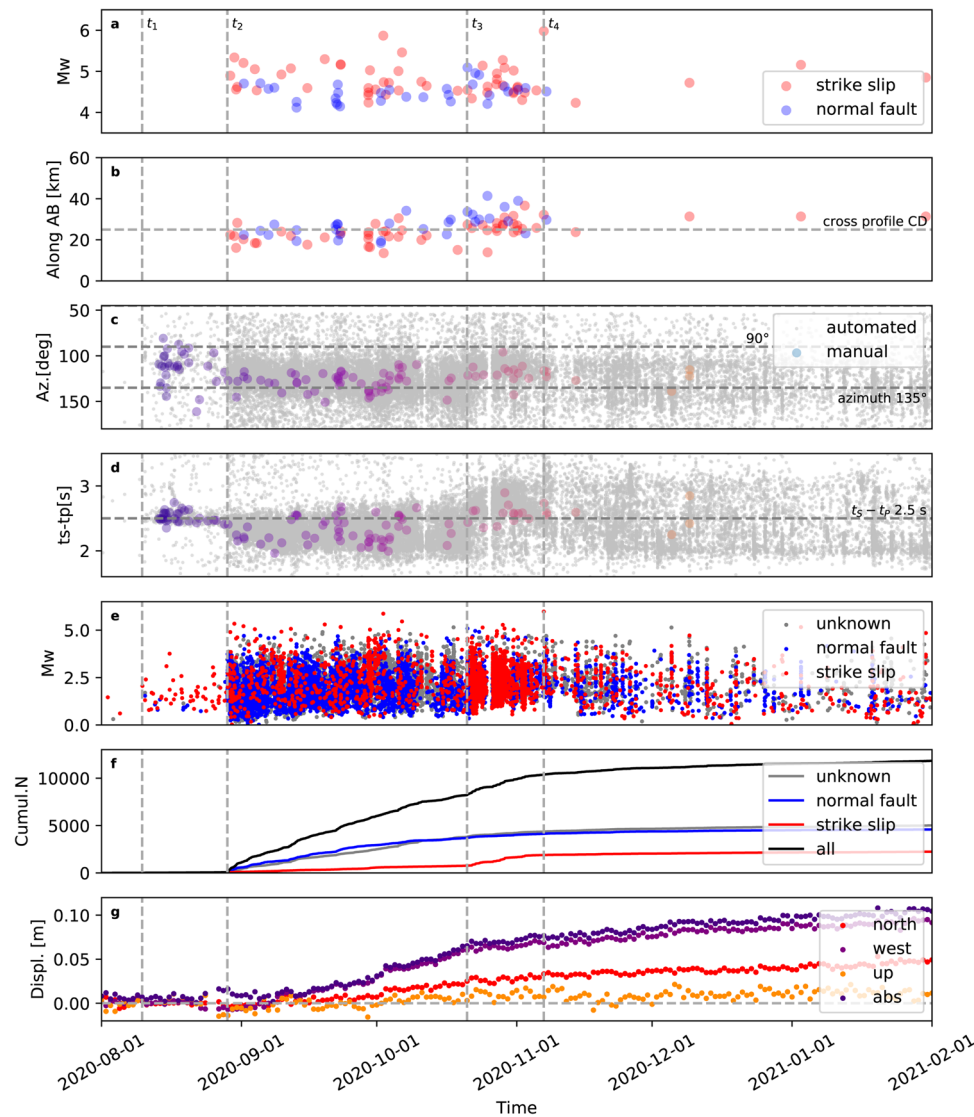
Fig. 4 Sequence timeline. The figure shows the results from different techniques: moment tensor inversion results (**a** magnitudes, and **b** horizontal projection along the profile AB in Fig. 2, colored according to the two predominant focal mechanisms); single station analysis at station JUBA (**c**, backazimuths of polarized P phases, and (**d**) differential S-P time as a proxy for the source-receiver distance, colored based on automated and manual picks); template matching (**e**, magnitude, and **f** cumulative number of detections, colored based on the focal mechanism of the template events, only events with threshold at 12 times the MAD and cross correlation values above 0.55 are shown, see Supplementary Note 7); observations from the GNSS station DAL5 (**g** cumulative displacements since the unrest start).) Dashed lines mark the onset of different phases of seismicity: early weak seismicity (t_1, August 10, 2020), increased seismicity (t_2, August 29, 2020), new burst of strike-slip earthquakes (t_3, October 21, 2020) and seismicity drop (t_4, November 6, 2020).

pressure. Alternatively, this could be the most likely timing for a submarine eruption. At Bardardarbunga, the growth of a lateral dike was slowed down at the time of the fissure eruption[50], accompanied by a drop of seismicity rate[51]. The temporal evolution of sea surface temperature and roughness anomalies (Supplementary Note 11, Supplementary Fig. 17), recently used to detect submarine eruptions[52,53], do not conclusively show a heat source. Centroid depths are not accurate enough to judge whether the magma reached the seafloor, or not. At the end of the study period, by the beginning of February 2021, seismicity and deformation rate are substantially reduced, but still considerably larger than those in Phase 1. The later occurrence of a M 7.0 earthquake close to Elephant Island[2,3] and the reactivation of some moderate seismic activity at Bransfield in March 2021 may indicate some mutual tectonic influence over a broader region.

Discussion

The ground displacements observed at King George Island are too large to be explained by swarm earthquakes only, as these only accounts for 1–4% of the observed deformation amplitude (Supplementary Fig. 14). In addition to the seismic source, modeling the deformation data requires a large aseismic source, either in the form of aseismic slip along a broader normal fault system or a volumetric magmatic intrusion. There are several reasons to support the second scenario. The first is the distributed regional volcanism along the Bransfield Strait[4] and the presence of a low velocity volume beneath it, with abundance of partial melt[10,21]. The lateral migration resolved by our seismological analysis provides a second argument for dike-induced seismicity, which is often accompanied by migration of seismicity[38,50,51,54–57]. Double couple (DC) components are predominant in moment tensor (MT) solutions (accounting, in average, for $46 \pm 21\%$ of the moment release), but substantial non-DC

components are resolved for the vast majority of the earthquakes in the sequence (Supplementary Fig. 7). They are mostly characterized by positive isotropic (average $9 \pm 9\%$) and positive compensated linear victor dipoles (CLVD, average $43 \pm 21\%$) terms, suggesting that opening tensile failures accompany shear faulting. MT solutions further support the magmatic origin of the swarm. Opening tensile components are consistent with a magmatic intrusion, although in other case they occur aseismically[51]. The resolved focal mechanisms are also typical for seismicity controlled by dike propagation[38,50,51,56,58]. Finally, reproducing the observed displacement amplitudes by shear faulting would require the aseismic failure of a large (~40 km long) normal fault segment, with an equivalent magnitiude Mw 7. However, the spatial extent of the deformation signal and the modeling of InSAR data constrain the length of the deformation source to be shorter (~20 km).

The magmatic intrusion must be fed by a deeper reservoir, which should presumably lay at least at ~20 km depth below a region located NE off the Orca seamount, where the first seismic sign of unrest appeared. The depletion of such reservoir should produce a deformation signal with opposite sign compared to the dike opening, as recently observed offshore Mayotte, Comoro Islands[58]. A low velocity region has been imaged in the mantle wedge beneath the South Shetland Islands and interpreted in terms of widespread partial melting[10], providing a huge reservoir of magma. Based on the fit of geodetic data the estimated magma volume of the intrusion varies between 0.26-0.56 km³, either considering the dike effect only, or including an additional deeper depleting source. Such volumetric intrusions are expected to trigger seismicity with a cumulative scalar moment of $0.69–1.86 \times 10^{18}$ Nm[59] (equivalent to Mw 5.9-6.1), consistent with our estimates (~3.46×10^{18} Nm, Mw 6.3). The estimated magma volume (0.26-0.56 km³) and horizontal dike length (20 km), makes the Orca magmatic unrest episode the largest to be geophysically monitored in Antarctica ever, that also triggered the largest earthquake swarm ever observed in that region.

A vertical magmatic intrusion crossing the whole crust is hypothesized in phase 2, similarly to the Mayotte case, where such migration was tracked through a thicker crust[58]. In both cases, the upward propagation of magma within an extensional tectonic domain triggers earthquakes with strike-slip to oblique focal mechanisms. Tracking their spatiotemporal evolution allows to reconstruct the path of magma ascent[58]. At Mayotte, this path could be tracked to the seafloor[58], pointing to the location where a new seafloor volcano was found[60]. Here, conversely, strike-slip earthquakes are confined deeper than ~8 km depth. Shallow seismicity is mostly characterized by NE-SW oriented normal faulting mechanisms, which are expected to occur above a forming sub-vertical dike[37,38,54,57,61]. It is not clear, though, whether the magma intrusion reached the Bransfield Strait seafloor or not. For sure, the occurrence of the Mw 6.0 earthquake abruptly changed the seismicity rate, which is an indication of pressure loss in the intrusion.

A unique aspect of the Bransfield unrest is that it occurs in a very specific rifting environment, which is experiencing the transition from continental to oceanic crust. The observed intrusion and seismicity represent a specific stage of this process and are controlled by the interplay of magmatic and tectonic processes over different scales. The unrest demonstrates how long-term steady extension processes testified by GNSS observations[35] can occasionally alternate with short term, fast intrusion and rifting processes, providing magma paths through the entire crust over few days and lasting over months. While volcanic processes are the driver of local seismicity, they are favored by the long term tectonic settings, which control the rifting and oceanic formation processes at a larger scale. The unrest also testifies how episodic intrusions through the crust allows transferring large magma volumes from the upper mantle to the seafloor, as a stage of the formation of elongated volcanic structures, which are typical bathymetric features along the Bransfield Strait[22].

Methods

Single station analysis: earthquake detection and localization. We tackle the limited detection capability of global networks in the Antarctic region by implementing different single station approaches, substantially augmenting the number of detected earthquakes during the sequence of volcano-tectonic earthquakes. We apply the Lassie detector (https://gitext.gfz-potsdam.de/heimann/lassie) and the PhaseNet[30] picker algorithm to continuous recordings at the closest seismic stations, JUBA and R4DE2, to detect signals of weaker earthquakes and pick P and S earthquake arrival times. Details of the two algorithms are provided in the Supplementary Information. Differential times and P wave polarization attributes are estimated[58] to perform a single station location. Differential S–P times provide information on the distance between the considered station and earthquake hypocenters and are obtained independently with two different techniques and for both JUBA and R4DE2 stations (Fig. 3, Supplementary Fig. 4). The source back-azimuth can be estimated from the P wave signal, whenever its particle motion is highly linearly polarized. With the distance and backazimuth, and knowing the absolute location of the largest events, we can locate with a single-station approach. We correct the cloud of single-station locations shifting their average to match the average centroid locations from the regional moment tensor inversion. PhaseNet has been additionally applied to a few more stations at larger distances, which detect much fewer events.

Moment tensor inversion. The moment inversion provides stable and high quality results for 84 earthquakes (Supplementary Dataset 2), out of 128 identified by global catalogs. We perform both deviatoric and full moment tensor inversions. Results are similar in terms of magnitude, depth and geometry of the double couple component, so that we discuss here full moment tensor solutions only, as they allow to interpret also the isotropic components. The full moment tensor inversion is performed using the Grond software[29]. We fit regional broadband seismic data from seismic stations shown in Supplementary Fig. 1, considering those located at epicentral distances up to 2,500 km. Synthetic seismograms are computed[62] using a regional model at distances below 500 km and an average model with oceanic crust at larger distances (Supplementary Fig. 2). Full waveform displacement data are fitted in the time domain for 3-components (vertical, radial, transversal). To maximize the signal-to-noise ratio and ensure a good data fit using simplified 1D models, we apply the following bandpass filters, depending on station distance and component: for far distance stations (500–2,500 km distance), we use a bandpass filter 0.01–0.03 Hz for vertical components and 0.02–0.03 Hz for horizontal components, while for closer distances (below 500 km), we employ a bandpass filter 0.015–0.04 Hz for vertical component and 0.02–0.04 Hz for horizontal components. Data have been visually inspected for all events, removing where necessary saturated, noisy or incomplete traces. Grond was setup to perform 56,000 iterations, resolving simultaneously centroid location, centroid depth, centroid time and the 6 independent moment tensor components. We use an impulsive source time function with 1 s duration. The inversion using all data (which lead to best solution estimates) is accompanied by simultaneous inversions using 100 bootstrap chains, where the available data contribute with different random weights. The bootstrap chains carry out independent optimizations, thus providing 100 additional solutions for each earthquake; these solutions are finally used to estimate mean solutions and parameter uncertainties.

Earthquake classification. Earthquake classification is performed on the base of the resolved moment tensors for 84 earthquakes. We use a density based clustering software (Seiscloud[31]), which implements the DBSCAN algorithm[63]. Earthquakes are clustered upon the similarity of their focal mechanisms, i.e. using the normalized Kagan angle[64] as metric. Considering that many solutions include opening tensile components with a common NW-SE orientation, classifying upon the double couple term is much more efficient for this dataset, compared to using a metrics based on the full moment tensor components[31]. We select the DBSCAN parameters $Nmin = 10$ and $\varepsilon = 0.12$, so that a cluster is formed whenever for a given earthquake there are at least 10 other earthquakes, with a normalized Kagan angle equal or smaller than 0.12 (corresponding to a Kagan angle equal or smaller than ~15°). We force unclustered events to the cluster whose focal mechanisms are, in average, more similar to its focal mechanism[31].

Template matching. To enhance the number of detected events during the seismo-volcanic sequence and to associate smaller events with larger ones with a known focal mechanism, we apply a phase match filtering[32], which is designed to detect seismicity from the cross-correlation of continuous data and templates. The processing consists of performing the single-channel cross-correlation for the event and then stack all individual cross-correlations into a network function. A

threshold is applied to the resulting stacked function to declare a positive detection. Generally the threshold is fixed N times above the median absolute deviation (MAD). Template matching techniques can augment the number of detected earthquakes by a factor 5-10[65–67]. The PyMPA analysis (https://github.com/avuan/PyMPA37) is applied to JUBA daily three-component continuous waveforms from 1 August 2020 to 31 January 2021. We use the combination of the MT inversion solutions obtained in this study and the original hypocentral solutions provided by Global CMT[2,3], GEOFON (http://geofon.gfz-potsdam.de/, last accessed 1.3.2021) and USGS (https://earthquake.usgs.gov/, last accessed 1.3.2021) as input catalogue for the template matching. It consists of 128 earthquakes, in the Mw range from 4 to 6. Mw is obtained as a result of MT inversion, retrieved from the original catalogues or derived from mb using a suggested conversion relationship[68].

Due to data gaps of JUBA station recordings, seismic waveforms are missing for 5 seismic events of the composite catalogue, leading to 123 the number of useful templates. Data is resampled at 20 Hz, a bandpass filtering between 2 and 8 Hz is applied and the cross-correlation is calculated in time domain. Templates are trimmed using a 24 s data window, starting 12 s before the theoretical S wave arrival, computed using the ObsPy port[69] of the Java TauP Toolkit routines[70] and a suitable 1D-model[7,21]. The selected time windows guarantee to consider P and S picks arrival travel times, a pre-event time window and an appropriate portion of signal after S wave arrival time.

The JUBA station correlograms are evaluated as a function of time, shifting sample by sample the template event window through continuous waveforms. We use 6 samples tolerance in detecting maximum cross-correlation amplitude for each channel. To declare candidate detections, we initially set the threshold at 8 times the MAD, and we impose at least two channels with cross-correlation values higher or equal to 0.4. When multiple templates exist for the same detection, we choose the template for which the normalized correlation coefficient is the greatest for determining the location and magnitude of the detected events[66]. PyMPA estimates the magnitude of the detected event by comparing its amplitude with that of the template, and assuming that a tenfold increase in ratio corresponds to a one-unit increase in magnitude. Finally, the 5 events missed as templates due to JUBA data gaps are added in the template matching catalogue, getting a total number of 124,787 events. After the visual inspection for a subset of detections, we choose a minimum mean (i.e. mean of different components) cross correlation value of 0.40 and fix the threshold at 12 times the MAD to reduce uncertain associations, decreasing the number of detected events from 124,787 to 85,206 (Supplementary Dataset 3).

GNSS and InSAR data processing. GNSS data is provided by two stations (UYBA, DAL5) at King George Island. Collected GNSS data for the time period 1.1.2020 to 18.4.2021 are analysed using the Earth Parameter and Orbit System (EPOS) software[71] in units of 24 h. Together with up to 12 well distributed IGS core stations a GNSS network is formed. In the network processing all the stations are analysed with the same weight. Finally the network solutions are aligned to the IGS 3nd reprocessing combined daily coordinate product[72,73] to reduce the impact of datum effect. The coordinate results from the network solution have an accuracy better than 2 mm.

InSAR provides information on surface deformation along King George Island coastline. We use Small BAseline Subset (SBAS) InSAR time series analysis to estimate the ongoing deformation. All available Sentinel-1 data between November 2019 and January 2021, covering the study area, are collected to produce the cumulative deformation map. The Differential InSAR technique (DInSAR) is then implemented on the selected interferometric pairs to remove the topographic phase component and resolve the deformation. We enhance the quality of the final deformation map by removing the remaining DEM errors.

Further details on GNSS and InSAR data processing are provided in the Supplementary Information.

Modeling of GNSS and InSAR data. The theoretical displacements in the analyses were computed using the Python toolbox Pyrocko[28] either assuming a regional velocity model for the back-arc[4] (Supplementary Fig. 2) or a homogeneous half-space (Poisson's ratio $\nu = 0.25$, shear modulus $G = 24$ GPa) in the case of dislocation models[36]. The source models used in each analysis are described in the following paragraphs. Due to the limited availability of only two GNSS stations with unfavorable distribution, roughly at the same backazimuth, we do not run an inversion but search for a best fitting set of model parameters with centroid locations along profile AB (Fig. 2) using a grid search approach with an L2-norm (see following subsections). Afterwards, we compare the best fitting theoretical displacement models found in the grid searches to InSAR observations, to overcome the limited GNSS observations and constrain the extent of the dike (see subsection Insights into dike extent from InSAR observations).

Geodetic modeling of co-seismic displacements. We computed the theoretical surface displacements at the GNSS stations UYBA and DAL5, based on the back-arc model, caused by the cumulative effects of moment tensor point sources, as derived in our study (Fig. 2). The theoretical cumulative displacement of the

seismic events can only explain 1–3 mm (~1–4%) of the horizontal displacement observed at the two stations, while the direction of the horizontal displacement coincides with the observation. The vertical displacement of the models is negligible.

A hypothetical single aseismic event, that could account for the observed cumulative displacement at the two GNSS stations, was modeled with the back-arc velocity model. The source angles of the assumed pure normal faulting event (rake of −90°) are fixed to a dip of 45° and a strike of 225°, corresponding to the alignment of the studied epicenters. The width and the length of the fault were estimated via empirical relations[59] (Supplementary Tab. 2).

Geodetic modeling of the assumed magmatic source. For the geodetic modeling of the magmatic sources we considering extended sources, point sources, and a combination of both sources. For the point sources, we assume purely volumetric sources[74]. The extend sources are represented by homogeneous half-space dislocation models[36]. We set up grid searches over the model parameters space to fit the orientation and magnitude of the two GNSS vectors, using an L2 norm. The parameter space of the grid search is free at the beginning, but refined during the analyses. The grid searches are run for single source intrusions (extended source or point source) as well as for the summed displacement of a depleting magma chamber (depleting point source) and an opening dike (extended source); results are summarized in Supplementary Tabs. 2, 3.

We first model a single volumetric point source by initially searching for the best fitting set of location, depth, and volume change. Due to the point source symmetry and the similar backazimuth of the two GNSS stations, we observe trade-offs between volume change, depth and the distance to the stations while the models are moving away perpendicular to profile AB. To overcome this ambiguity, we require the location to be on the profile AB. The same constraint is later used for all tested surface displacement models (Supplementary Tab. 2).

Next, the best point source location is used as the fixed centroid of an extended dislocation source. We perform another grid search to find the best fitting rectangular dislocation source parameters (fault length, fault width, fault strike, fault dip, and intruding volume), assuming a pure tensile opening. The amount of opening is calculated from the fault area and the intruding volume. The extended model provides a better fit to the observed deformation (Supplementary Tab. 3).

By adding a secondary source to our models we test whether an additional depleting magma chamber below the dike can better explain the observed displacement. We assume that the magma chamber is located close to the first seismic activity, here represented by the average location of strike-slip templates in phase 2 and a depth of 20 km. We model its contribution to the surface displacement, by assuming that the volume of the dike is equal to the volume depleting source below it. When using the best point source model location, we cannot model the observations better by adding a depleting source. Here we tested a model with two point sources (one depleting and another inflating), and another one with an extended (dike) source centered at the best point source location plus a deeper depleting source. In both cases, the data fit was not improved. To better fit the data, we have to allow the centroid location to move along profile AB in the grid search. For the free grid search the unfavorable station configuration leads to a very small dike length of the best fitting model (Supplementary Tab. 2). Due to the scaling of the opening with length/width and the volume of the dike, this leads to unreasonable opening estimates for the dike. To resolve this ambiguity and constrain the dike extent we consider displacements from InSAR observations in the following paragraph.

Insights into dike extent from InSAR observations. We constrain the length of the dike by analyzing sparse InSAR data over the time period of July 2020 to February 2021. Although the data is limited to the coastal regions due to ice fields on the island, it covers a broader region and helps to distinguish between dikes of different spatial extents and centroid locations. First, we search for best fitting displacement models (the combination of an extended source and a depleting point source) with fixed dike lengths varying between 5 km and 40 km, using the same grid search approach as before. Then, we compare the modeled displacements to observed downsampled InSAR displacement steps (Supplementary Fig. 16). We downsample InSAR observation based on an adaptive quadtree sampling method[75], that can subsample data points regardless of whether spaced regularly (e.g., grid data) or irregularly (e.g., PS data point in our case). The method splits data points into the sample grids (or polygon) of different sizes determined by displacement gradient. The process iterates until the displacement variance within a polygon is below a defined threshold. Based on the models we found that the InSAR observations rule out larger dike lengths (e.g. 40 km) and a substantial dike propagation towards SW (Supplementary Fig. 16). Both would contradict the observed InSAR derived displacements. A dike to the NE of the Orca Volcano is in agreement with the normal faulting events within the seismic series. By considering the distribution of the normal faulting events, and the fit to both the GNSS and the InSAR data we conclude that the sub-vertical dike has a length of approximately 20 km. The according preferred model is given in Supplementary Tab. 2. The

difference in the scale of modeled and observed displacements closer to the source (see difference in color scale in Supplementary Fig. 16d), is caused by using UYBA as a reference station, which introduces an offset of approximately 2 cm in the line-of-sight displacement (Supplementary Fig. 15).

Data processing and analysis of sea surface data. The temporal evolution of sea surface temperature and roughness within the study area (Supplementary Fig. 17) are here obtained from remote sensing data, by Advanced Very High Resolution Radiometer (AVHRR), high resolution optical (Sentinel-2 and Landsat-8) and synthetic aperture radar (SAR) (Sentinel-1). To identify possible effects of a hypothetical submarine eruption at Orca Seamount on the sea surface, time series of sea surface temperature (SST) data were first analyzed. Thereby, the NOAA Optimum Interpolation 1/4 Degree Daily Sea Surface Temperature (OISST) Analysis, Version 2 product[76] was used. This SST dataset has a spatial grid resolution of 0.25 (1/4) degree and temporal resolution of 1 day. This SST dataset is based on Advanced Very High Resolution Radiometer (AVHRR) satellite data. The operational Navy AVHRR Multi-Channel SST algorithm is used. In situ data from ships and buoys are used as additional information. Thereby, a large-scale adjustment of satellite biases with respect to the in situ data is included. An optimum interpolation (OI) technique is used to fill data gaps. Besides the SST, this product also provides information about the sea ice coverage. For areas covered by sea ice, SST is estimated from sea ice concentration datasets from NOAA NCEP. Data from high resolution optical (Sentinel-2 and Landsat-8) and synthetic aperture radar (SAR) (Sentinel-1) sensors were analyzed in order to search for floating pumice rafts, previously observed after other submarine eruptions[52,53,61]. Almost all optical imagery were cloudy and no optical imagery were available during the dark period of the Antarctic winter. Analysis of SAR data, which is independent of the weather and sunlight showed also no clear evidence for localized roughness anomalies. The area of interest was often affected by high waves (rough water surface) and during the winter large areas of the region were covered by sea ice. For example, Sentinel-1 SAR data showed complete sea ice coverage between August 28 and September 9, 2020.

Data availability

Seismic data used in this study are available at IRIS (Incorporated Research Institutions for Seismology, https://service.iris.edu/), GEOFON (GEO-ForschungsNetz, https://geofon.gfz-potsdam.de/waveform/webservices/), ORFEUS EIDA (Observatories and Research Facilities for European Seismology - European Integated Data Archive, https://www.orfeus-eu.org/data/eida/webservices/) and Raspberry Shake Project (https://manual.raspberryshake.org/fdsn.html#fdsnwebservices) FDSN web services. The list of seismic networks is provided and acknowledged in the Supplementary Material. Seismic catalogs produced in this study[77] are provided as Supplementary Datasets. Geodetic data are available at the web facilities of the Nevada Geodetic Laboratory, at the University of Nevada, Reno[78].

Code availability

All software used in this work is open source. The codes used to generate individual results are available through the contact information from the original publications. Requests for further materials should be directed to S.C. (simone.cesca@gfz-potsdam.de).

References

1. Loureiro Olivet, J. et al. A seismic swarm at the Bransfield Rift, Antarctica. *J. South Am. Earth Sci* **111**, 103412 (2021).
2. Dziewonski, A. M. et al. Determination of earthquake source parameters from waveform data for studies of global and regional seismicity. *J. Geophys. Res.* **86**, 2825–2852 (1981).
3. Ekström, G. et al. The global CMT project 2004-2010: Centroid-moment tensors for 13,017 earthquakes. *Phys. Earth Planet. Inter.* **200-201**, 1–9 (2012).
4. Dziak, R. P. et al. Tectonomagnetic activity and ice dynamics in the Bransfield Strait back-arc basin, Antarctica. *J. Geophys. Res.* **115**, B01102 (2010).
5. Kanao, M. Seismicity in the Antarctic continent and surrounding ocean. *Open J. Earth. Res* **3**, 5–14 (2014).
6. Kaminuma, K. A possibility of earthquake swarms around Orca sea mount in the Bransfield Strait, the Antarctic. In *Proceedings of the Joint International Seminar. Recent Interests on Antarctic Earth Sciences of Korea and Japan* (Y. Kim & B. K. Khim Eds.), 23-34 (2001).
7. Robertson Maurice, S. D. et al. Seismicity and tectonics of the South Shetland Islands and Bransfield Strait from a regional broadband seismograph deployment. *J. Geophys. Res.* **108**, B10, 2461 (2003).
8. Lawver, L. A. et al. Distributed, active extension in Bransfield Basin, Antarctic Peninsula: evidence from multibeam bathymetry. *GSA Today* **6**, 11, 1–6 (1996).
9. Grácia, E. et al. Morphostructure and evolution of the central and eastern Bransfield Basins (NW Antarctic Peninsula). *Mar. Geophys. Res.* **18**, 429–448 (1996).
10. Parera-Portell, J. A. et al. Structure of the crust and upper mantle beneath the Bransfield Strait (Antarctica) using P receiver functions. *Tectonophysics* **802**, 228744 (2021).
11. Keller, R. A. et al. Geochemistry of back arc volcanism in Bransfield Strait, Antarctica: subducted contributions and along-axis variations. *J. Geophys. Res.* **107**, B8, 2171 (2002).
12. Christeson, G. L., Barker, D. H. N., Austin, J. A. Jr. & Dalziel, W. D. Deep crustal structure of Bransfield Strait: Initiation of a back arc basin by rift reactivation and propagation. *J. Geophys. Res.* **108**, 2492 (2003). B10.
13. Forsyth, D. W. Fault plane solutions and tectonics of the South Atlantic and Scotia Sea. *J. Geophys. Res.* **80**, 1429–1443 (1975).
14. Pelayo, A. M. & Wiens, D. A. Seismotectonics and relative plate motions in the Scotia Sea region. *J. Geophys. Res.* **94**, 7293–7320 (1989).
15. Grácia, E., Canals, M., Farran, M. L., Sorribas, J. & Pallas, R. Central and eastern Bransfield basins (Antarctica) from high-resolution swathbathymetry data. *Antarct. Sci.* **9**, 168–180 (1997).
16. Keller, R. A., Fisk, M. R., White, W. M. & Birkenmajer, K. Isotopic and trace element constraints on mixing and melting models of marginal basin volcanism, Bransfield Strait, Antarctica. *Earth Planet. Sci. Lett.* **111**, 287–303 (1992).
17. Rodrigo, C., Blamey, J. M., Huhn, O. & Provost, C. Is there an active hydrothermal flux from the Orca seamount in the Bransfield Strait, Antarctica? *Andean Geology* **45**, 344–356 (2018). 3.
18. Dietrich, R. et al. ITRF coordinates and plate velocities from repeated GPS campaigns in Antarctica - An analysis based on different individual solutions. *J. Geod.* **74**, 756–766 (2001).
19. Barker, D. H. N., Christenson, G. L. & Austin, J. A. Backarc basin evolution and cordilleran orogenesis: Insights from new ocean-bottom seismograph refraction profiling in Bransfield Strait, Antarctica. *Geology* **31**, 107–110 (2003).
20. Grad, M., Shiobara, H., Janik, T., Guterch, A. & Shimamura, H. Crustal model of Bransfield rift, west Antarctica, from detailed OBS refraction experiments. *Geophys. J. Int* **130**, 506–518 (1997).
21. Vuan, A., Robertson Maurice, S. D., Wiens, D. A. & Panza, G. F. Crustal and upper mantle S-wave velocity structure beneath the Bransfield Strait (West Antarctica) from regional surface wave tomography. *Tectonophysics* **397**, 241–259 (2005). 3–4.
22. Schreider, Al. A., Schreider, A. A. & Evsenko, E. I. The Stages of the Development of the Basin of the Bransfield Strait. *Oceanology* **54**, 365–373 (2014). 3.
23. Hatzky, J. *The Orca Seamount Region, Antarctica*, in *Sound Images of the Ocean in Research and Monitoring* (Wille, P. W., ed.), (Springer, Berlin Heidelberg New York, 2005).
24. Dählmann, A. et al. Hot vents in an ice-cold ocean: indications for phase separation at the southernmost area of hydrothermal activity, Bransfield Strait, Antarctica. *Earth Planet. Sci. Lett.* **193**, 381–394 (2001).
25. Klinkhammer, G. et al. Discovery of new hydrothermal vent sites in Bransfield Strait, Antarctica. *Earth Planet. Sci. Lett.* **193**, 395–407 (2001).
26. Fisk, M. Volcanism in the Bransfield Strait, Antarctica. *J. South American Earth Sci* **3**, 91–101 (1990).
27. Almendros, J. et al. BRAVOSEIS: Geophysical investigation of rifting and volcanism in the Bransfield strait, Antarctica. *J. South American Earth Sci* **104**, 102834 (2020).
28. Heimann, S. et al. Pyrocko - an open-source seismology toolbox and library. *GFZ Data Services* https://doi.org/10.5880/GFZ.2.1.2017.001 (2017).
29. Heimann, S. et al. Grond – A probabilistic earthquake source inversion framework. *V. 1.0. GFZ Data Services* https://doi.org/10.5880/GFZ.2.1.2018.003 (2018).
30. Zhu, W. & Beroza, G. C. PhaseNet: a deep-neural-network-based seismic arrival-time picking method. *Geophys. J. Int* **216**, 261–273 (2019). 1.
31. Cesca, S. Seiscloud, a tool for density-based seismicity clustering and visualization. *J. Seismol.* **24**, 443–457 (2020).
32. Vuan, A., Sugan, M., Amati, G. & Kato, A. Improving the Detection of Low-Magnitude Seismicity Preceding the Mw 6.3 L'Aquila Earthquake: Development of a Scalable Code Based on the Cross-Correlation of Template Earthquakes. *Bull. Seismol. Soc. Am* **108**, 471–480 (2018). 1.
33. Shimizu, H., Ueki, S. & Koyama, J. A tensile-shear crack model for the mechanism of volcanic earthquakes. *Tectonophysics* **144**, 287–300 (1987). 1-3.
34. Cesca, S. et al. Seismicity at the Castor gas reservoir driven by pore pressure diffusion and asperities loading. *Nat. Comm* **12**, 4783 (2021).

35. Taylor, F. W. et al. Kinematics and segmentation of the South Shetland Islands-Bransfield basin system, northern Antarctic Peninsula. *Geochem. Geophys. Geosyst.* **9**, 4 (2008).

36. Okada, Y. Surface Deformation due to Shear and Tensile Faults in a Half-Space. *Bull. Seismol. Soc. Am* **75**, 1135–1154 (1985).

37. Hill, D. P. A model for earthquake swarms. *J. Geophys. Res.* **82**, 1347–1352 (1977). 8.

38. Passarelli, L., Rivalta, E., Cesca, S. & Aoki, Y. Stress changes, focal mechanisms, and earthquake scaling laws for the 2000 dike at Miyakejima (Japan). *J. Geophys. Res. Solid Earth* **120**, 4130–4145 (2015).

39. Rivalta, E., Taisne, B., Bunger, A. P. & Katz, R. F. A review of mechanical models of dike propagation: Schools of thought, results and future direction. *Tectonophysics* **638**, 1–42 (2015).

40. Dahm, T. Numerical simulations of the propagation path and the arrest of fluid-filled fractures in the Earth. *Geophys. J. Int.* **141**, 623–638 (2000).

41. Maccaferri, F., Bonafede, M. & Rivalta, E. A quantitative study of the mechanisms governing dike propagation, dike arrest and sill formation. *J. Volc. Geoth. Res.* **208**, 39–50 (2011).

42. Taisne, B., Tait, S. & Jaupart, C. Conditions for the arrest of a vertical propagating dyke. *Bull. Volcanol.* **73**, 191–204 (2011). 2.

43. Kervyn, M. et al. Volcano load control on dyke propagation and vent distribution: Insights from analogue modeling. *J. Geophys. Res. Solid Earth* **114**, B3 (2009).

44. Dahm, T. On the shape and velocity of fluid-filled fractures in the Earth. *Geophys. J. Int.* **142**, 181–192 (2000).

45. Klein, F. W., Koyanagi, R. Y., Nakata, J. S. & Tanigawa, W. R. The seismicity of Kilauea's magma system. *Volcanism in Hawaii* **2**, 1019–1185 (1987).

46. Rubin, A. M., Gillard, D. & Got, J.-L. A reinterpretation of seismicity associated with the January 1983 dike intrusion at Kilauea Volcano, Hawaii. *J. Geophys. Res. Solid Earth* **103**, 10003–10015 (1998). B5.

47. Maccaferri, F., Rivalta, E., Passarelli, L. & Aoki, Y. On the mechanisms governing dike arrest: Insight from the 2000 Miyakejima dike injection. *Earth Planet. Sci. Lett.* **434**, 64–74 (2016).

48. Xu, W., Jónsson, S., Corbi, F. & Rivalta, E. Graben formation and dikearrest during the 2009 Harrat Lunayyir dike intrusion in Saudi Arabia: Insights from InSAR, stress calculations and analog experiments. *J. Geophys. Res. Solid Earth* **121**, 2837–2851 (2016).

49. Bonaccorso, A., Aoki, Y. & Rivalta, E. Dike propagation energy balance from deformation modeling and seismic release. *Geophys. Res. Lett.* **44**, 5486–5494 (2017). 11.

50. Sigmundsson, F. et al. Segmented lateral dyke growth in a rifting event at Bárðarbunga volcanic system, Iceland. *Nature* **517**, 191–195 (2015).

51. Agustsdottir, T. et al. Strike-slip faulting during the 2014 Bárðarbunga-Holuhraun dike intrusion, central Iceland. *Geophys. Res. Lett* https://doi.org/10.1002/2015GL067423 (2016).

52. Jutzeler, M. et al. On the fate of pumice rafts formed during the 2012 Havre submarine eruption. *Nat Comm* **5**, 3660 (2014).

53. Brandl, P. A. et al. The 6–8 Aug 2019 eruption of 'Volcano F' in the Tofua Arc, Tonga. *J. Volcanol. Geotherm. Res.* **390**, 106695 (2020).

54. Einarsson, P., & Brandsdóttir, B., Seismological evidence for lateral magma intrusion during the July 1978 deflation of the Kraflavolcano in NE Iceland. (No. UI-79-9-7), University of Iceland, Reykjavik, IS, https://doi.org/10.2172/890964 (1978).

55. Belachew, M. et al. Comparison of dike intrusions in an incipient seafloor-spreading segment in Afar, Ethiopia: Seismicity perspectives. *J. Geophys. Res* **116**, B06405 (2011).

56. Belachew, M., Ebinger, C. & Coté, D. Source mechanisms of dike-induced earthquakes in the Dabbahu-Manda Hararo rift segment in Afar, Ethiopia: implications for faulting above dikes. *Geophys. J. Int* **192**, 907–917 (2013). 3.

57. Grandin, R. et al. Seismicity during lateral dike propagation: Insights from new data in the recent Manda Hararo-Dabbahu rifting episode (Afar, Ethiopia). *Geochem. Geophys. Geosyst.* **12**, Q0AB08 (2011).

58. Cesca, S. et al. Drainage of a deep magma reservoir near Mayotte inferred from seismicity and deformation. *Nat. Geosci.* **13**, 87–93 (2020).

59. White, R. & McCausland, W. Volcano-tectonic earthquakes: a new tool for estimating intrusive volumes and forecasting eruptions. *J. Volcanol. Geotherm. Res.* **309**, 139–155 (2016).

60. Feuillet, N. et al. Birth of a large volcano offshore Mayotte through lithosphere-scale rifting. *AGU Fall Meeting Abstracts* **2019**, V52D–01 (2019).

61. Passarelli, L. et al. Magmatic or Not Magmatic? The 2015–2016 Seismic Swarm at the Long-Dormant Jailolo Volcano, West Halmahera, Indonesia. *Front. Earth Sci.* **6**, 79 (2016).

62. Heimann, S. et al. A Python framework for efficient use of pre-computed Green's functions in seismological and other physical forward and inverse source problems. *Solid Earth* **10**, 1921–1935 (2019). 6.

63. Ester, M. et al. A density-based algorithm for discovering clusters in large spatial databases with noise. In *KDD'96: Proceedings of the Second International Conference on Knowledge Discovery and Data Mining* **1996**, 226–231 (1996). August.

64. Kagan, Y. Y. 3-D rotation of double-couple earthquake sources. *Geophys. J. Int* **106**, 709–716 (1991). 3.

65. Shelly, D., Beroza, G. & Ide, S. Non-volcanic tremor and low-frequency earthquake swarms. *Nature* **446**, 305–307 (2007).

66. Kato, A. et al. Propagation of slow slip leading up to the 2011 Mw 9.0 Tohoku-oki earthquake. *Science* **335**, 705–708 (2012).

67. Sugan, M., Kato, A., Miyake, H., Nakagawa, S. & Vuan, A. The preparatory phase of the 2009 Mw 6.3 L'Aquila earthquake by improving thedetection capability of low magnitude foreshocks. *Geophys. Res. Lett.* **41**, 6137–6144 (2014).

68. Di Giacomo, D. et al. ISC-GEM: Global Instrumental Earthquake Catalogue (1900–2009), III. Re-computed MS and mb, proxy MW, final magnitude composition and completeness assessment. *Phys. Earth Planet. Int* **239**, 33–47 (2015).

69. Krischer, L. et al. ObsPy: A bridge for seismology into the scientific Python ecosystem. *Comput. Sci. Discov* **8**, 014003 (2015). 1.

70. Crotwell, H. P., Owens, T. J. & Ritsema, J. The TauP Toolkit: Flexible seismic travel-time and ray-path utilities. *Seismol. Res. Lett.* **70**, 154–160 (1999).

71. Gendt, G., et al. GFZ Analysis Center of IGS - Annual Report for 2013, 1–10 (2013).

72. Rebischung, P., Ray, J., Benoist, C., Metivier, L. & Altamimi, Z. Error Analysis of the IGS repro2 Station Position Time Series. *AGU Fall Meeting Abstracts* **2015**, 13 (2015).

73. Altamimi, Z., Rebischung, P., Métivier, L. & Collilieux, X. ITRF2014: A new release of the International Terrestrial Reference Frame modeling nonlinear station motions. *J. Geophys. Res. Solid Earth* **121**, 6109–6131 (2016). 8.

74. Mogi, K. Relations between the eruptions of various volcanoes and the deformations of the ground surfaces around them. *Earthq. Res. Inst* **36**, 99–134 (1958).

75. Decriem, J. et al. The 2008 May 29 earthquake doublet in SW Iceland. *Geophys. J. Int* **181**, 1128–1146 (2010). 2.

76. Reynolds, R. W., Banzon, V. F., & N. O. A. A. CDR Program. NOAA Optimum Interpolation 1/4 Degree Daily Sea Surface Temperature (OISST) Analysis, Version 2. NOAA National Centers for Environmental (2008).

77. Cesca, S. et al. Seismic catalogs of the 2020-2021 seismic swarm at the Bransfield Strait, Antarctica, https://doi.org/10.5281/zenodo.6363640 (2022)

78. Blewitt, G., Hammond, W. C. & Kreemer, C. Harnessing the gps data explosion for interdisciplinary science. *Eos* **99**, 4872–4886 (2018).

79. Bird, P. An updated digital model of plate boundaries. *Geochem., Geophys., Geosyst.* **4**, 3 (2003).

80. Ryan, W. B. F. et al. Global Multi-Resolution Topography (GMRT) synthesis data set. *Geochem. Geophys. Geosyst.* **10**, Q03014 (2009).

Acknowledgements

Author contributions

S.C. coordinated this project, conceived the manuscript and figures and analysed, modeled and interpreted seismological data. S.C. and M.S. performed single station analysis. M.S. and A.V. performed automated picking and template matching. S.C., L.R., G.P. and S.H. performed the moment tensor inversion. G.P. assessed the seismic data quality. Z.D. processed and analysed GNSS data. S.V. processed InSAR deformation data. S.P. analysed sea surface temperature and roughness data. P.N. performed the geodetic modeling. E.R. and T.D. contributed to the interpretation of results and discussion section. M. P. L., responsible for the installation of the AI network, collected and processed local seismic data. S.C., M.S., E.R., and T.D. drafted the manuscript. All authors reviewed the manuscript.

Funding

Competing interests

The authors declare no competing interests.

Additional information